CrossMark

³He-rich Solar Energetic Particle Observations at the *Parker Solar Probe* and near Earth

M. E. Wiedenbeck[1], R. Bučík[2,3], G. M. Mason[4], G. C. Ho[4], R. A. Leske[5], C. M. S. Cohen[5], E. R. Christian[6], A. C. Cummings[5], A. J. Davis[5], M. I. Desai[7], J. Giacalone[8], D. K. Haggerty[4], M. E. Hill[4], C. J. Joyce[9], A. W. Labrador[5], O. Malandraki[10], W. H. Matthaeus[11], D. J. McComas[9], R. L. McNutt, Jr.[4], R. A. Mewaldt[5], D. G. Mitchell[4], A. Posner[12], J. S. Rankin[9], E. C. Roelof[4], N. A. Schwadron[13], E. C. Stone[5], J. R. Szalay[9], S. D. Bale[14,15,16,17], A. W. Case[18], J. C. Kasper[18,19], K. E. Korreck[18], D. E. Larson[20], R. J. MacDowall[21], M. Pulupa[15], and M. L. Stevens[18]

[1] Jet Propulsion Laboratory, California Institute of Technology, Pasadena, CA 91109, USA; mark.e.wiedenbeck@jpl.nasa.gov
[2] Institüt für Experimentelle and Angewandte Physik, Christian-Albrechts-Universität zu Kiel, D-24188, Kiel, Germany
[3] Max-Planck-Institüt für Sonnensystemforschung, D-37077, Göttingen, Germany
[4] Johns Hopkins University, Applied Physics Laboratory, Laurel, MD 20723, USA
[5] California Institute of Technology, Pasadena, CA 91125, USA
[6] NASA Goddard Space Flight Center, Greenbelt, MD 20771, USA
[7] Southwest Research Institute, San Antonio, TX 78228, USA
[8] University of Arizona, Tucson, AZ 85721, USA
[9] Department of Astrophysical Sciences, Princeton University, Princeton, NJ 08544, USA
[10] National Observatory of Athens, IAASARS, Athens 15236, Greece
[11] Department of Physics and Astronomy, University of Delaware, Newark, DE 19716, USA
[12] NASA HQ, Washington, DC 20024, USA
[13] University of New Hampshire, Durham, NH 03824, USA
[14] Physics Department, University of California, Berkeley, CA 94720-7300, USA
[15] Space Sciences Laboratory, University of California, Berkeley, CA 94720-7450, USA
[16] The Blackett Laboratory, Imperial College London, London, SW7 2AZ, UK
[17] School of Physics and Astronomy, Queen Mary University of London, London E1 4NS, UK
[18] Smithsonian Astrophysical Observatory, Cambridge, MA 02138, USA
[19] Climate and Space Sciences and Engineering, University of Michigan, Ann Arbor, MI 48109, USA
[20] University of California at Berkeley, Berkeley, CA 94720, USA
[21] Solar System Exploration Division, NASA/Goddard Space Flight Center, Greenbelt, MD 20771, USA

Abstract

The Integrated Science Investigation of the Sun (IS⊙IS) instrument suite on the *Parker Solar Probe* (*PSP*) spacecraft is making in situ observations of energetic ions and electrons closer to the Sun than any previous mission. Using data collected during its first two orbits, which reached perihelion distances of 0.17 au, we have searched for ³He-rich solar energetic particle (SEP) events under very quiet solar minimum conditions. On 2019-110–111 (April 20–21), ³He-rich SEPs were observed at energies near 1 MeV nucleon^{-1} in association with energetic protons, heavy ions, and electrons. This activity was also detected by the Ultra-Low-Energy Isotope Spectrometer and the Electron, Proton, and Alpha Monitor instruments on the *Advanced Composition Explorer* (*ACE*) spacecraft located near Earth, 0.99 au from the Sun. At that time, *PSP* and *ACE* were both magnetically connected to locations near the west limb of the Sun. Remote sensing measurements showed the presence of type III radio bursts and also helical jets from this region of the Sun. This combination of observations is commonly associated with ³He-rich SEP acceleration on the Sun. AR 12738, which was located at Carrington coordinates from which numerous X-ray flares were observed over a period of more than 6 months, was identified as the source of the ³He-rich events. This region was also the source of several other SEP events detected at *PSP* or *ACE*. Aside from the period in 2019 April, IS⊙IS did not observe any other ³He-rich SEPs during orbits 1 and 2.

Unified Astronomy Thesaurus concepts: Solar energetic particles (1491); Solar activity (1475); Solar x-ray flares (1816)

Supporting material: animation

1. Introduction

Solar energetic particle (SEP) events are observed in the heliosphere when activity on the Sun causes the acceleration of ions and electrons to high energies. At least two different mechanisms are known to be capable of producing SEPs with energies in the MeV range. One of these involves energization by shocks or compressions that are driven by the ejection of mass and magnetic fields from the corona. The other is related to the energy release resulting from magnetic reconnection in solar flares. A brief review of the basic physics underlying these mechanisms has been given by Vainio & Afanasiev (2018). The investigation of the details of how these mechanisms operate has been an active field of research for decades and remains so today. Historically, SEP events produced by these two mechanisms have been referred to as "gradual" and "impulsive" events, respectively. While numerous subsequent studies have shown that these distinctions are not always clear and unambiguous, they can serve, nevertheless, as guides to the likely origin of specific events. For consistency with the large body of literature on SEP events, we will continue to use the terms gradual and impulsive, while admitting their limitations.

Various observational signatures have been identified that provide useful indications of which mechanism(s) are responsible for a particular event. These have been summarized in several review articles (Reames 1999; Kallenrode 2003; Mason 2007; Cliver 2009; Malandraki & Crosby 2018; Reames 2018). The most distinctive indicator that an event is impulsive is an enhancement of the ^{3}He/^{4}He ratio by several orders of magnitude over the solar wind value of $\sim 4 \times 10^{-4}$ (Geiss & Gloeckler 2003). In impulsive events, this ratio is commonly >0.1 and in extreme cases can be >10. Because the large enhancement of ^{3}He/^{4}He is often the best indicator that an event is impulsive, the term "^{3}He-rich" is often treated as synonymous with "impulsive." In this paper we use the two terms interchangeably.

Other key signatures of impulsive events include Fe/O $\sim 8\times$ the coronal value of ~ 0.13 (Reames 1999), relatively high He/H (~ 0.1), and association with type III radio bursts and energetic electron events. In addition, coronal mass ejections (CMEs) that are associated with large gradual events are commonly fast and wide, whereas those seen in connection with impulsive events tend to be slower and narrower, and sometimes are not observed at all. More recent work has also shown that impulsive events are often associated with narrow plasma jets from the active region (Wang et al. 2006; Nitta et al. 2015; Bučík et al. 2018, and references therein). Although the lack of sufficient information on associated eruptive phenomena such as CMEs can hinder the classification of some smaller events, Slocum et al. (2003) have shown that the signatures related to composition (e.g., ^{3}He/^{4}He, Fe/O) of the accelerated particles can still provide useful indications.

The characteristics of impulsive events observed near Earth are influenced not only by the processes that accelerate and release the particles from the Sun but also by transport processes (Wiedenbeck et al. 2015), including scattering on magnetic irregularities, velocity dispersion, adiabatic focusing, adiabatic deceleration, gradient and curvature drifts, and possible reacceleration by interplanetary shocks or compressions. When observed closer to the Sun, one would expect event characteristics to be less altered by these transport-related processes.

Section 2 introduces NASA's *Parker Solar Probe* (*PSP*) mission, which is now enabling impulsive SEP studies close to the Sun. Section 3 discusses some aspects of the energetic particle instrumentation that are particularly relevant for the present study. Section 4 presents an overview of the energetic particle activity that was observed in the MeV energy range during the first two *PSP* orbits. Section 5 reports energetic particle observations from the period 2019-110–111 (year-day) when IS☉IS detected the first ^{3}He-rich SEP events seen on *PSP*. Section 6 presents remote sensing observations of the solar activity associated with the 2019-110–111 events. Section 7 contains a discussion of the relationships among the various observations and their implications for the question of whether small ^{3}He-rich SEP events could be occurring more frequently than suggested by measurements made near Earth. Finally, Section 8 briefly summarizes the main results of this study.

2. *PSP*

On 2018 August 12 (2018-224), NASA launched the *PSP* spacecraft on a mission to investigate solar wind plasma, electric and magnetic fields, and energetic particles near the Sun (Fox et al. 2016). The mission design includes a series of close flybys of Venus to obtain gravitational assists that reduce the spacecraft's angular momentum about the Sun and lower its perihelion distance. Between Venus encounters, the spacecraft follows a simple Keplerian orbit. The first Venus flyby occurred on 2018-276 (October 3), and the second is scheduled for 2019-360 (December 26). Between these encounters, *PSP* reached perihelion distances of 0.17 au on 2018-309 (November 5), 2019-094 (April 4), and 2019–244 (September 1). During subsequent planned orbits, the perihelion is to be progressively reduced until it reaches 0.045 au ($\sim 10\,R_\odot$) in late 2024.

Included in the *PSP* payload is a two-instrument suite called the Integrated Science Investigation of the Sun (IS☉IS; McComas et al. 2016), designed for carrying out energetic particle studies. One of its objectives is to understand the physical processes responsible for particle acceleration and transport in impulsive events. The early *PSP* orbits are occurring in a period of very low solar activity during the minimum between Solar Cycles 24 and 25. At this time, there are very low backgrounds of SEPs from large events, unlike conditions expected closer to solar maximum when gradual events produce significant backgrounds, which can persist even during relatively inactive periods. The present quiet conditions are favorable for the study of the typically much less intense impulsive events.

Figure 1 shows the orbit of *PSP* between its first two Venus encounters, as well as the locations on 2019-110–111 of *PSP* and the *Advanced Composition Explorer* (*ACE*; Stone et al. 1998) spacecraft, which orbits the L1 Lagrange point 1.5×10^6 km sunward of Earth. At this time, the *Solar Terrestrial Relations Observatory* (*STEREO*) mission's *Ahead* spacecraft (*STEREO-A*; Driesman et al. 2008) was located near the Sun's east limb, as viewed from Earth, and was not magnetically connected to the region that produced the events seen at *PSP* and *ACE*. Parker-spiral magnetic field lines connecting *PSP* and *ACE* to the Sun are included in Figure 1. These are based on the solar wind speeds measured on 2019-110 by *PSP*'s SWEAP instrument (Kasper et al. 2016) and by *ACE*'s SWEPAM instrument (McComas et al. 1998). The speed measured at *ACE* early on 2019-110 was relatively slow, ~ 310–330 km s^{-1}, which would place *ACE*'s magnetic footpoint around W80. *PSP* was located at 0.46 au and longitude W60 as viewed from Earth. Solar wind speed measurements at *PSP* are only available sporadically for 2019-110. The data that are available indicate that the speed did not differ greatly from the nominal 400 km s^{-1}. A Parker spiral for this speed would connect to a footpoint located $\sim 30°$ west of *PSP*, which would place it on the west limb, close to the *ACE* footpoint.

The figure also indicates the heliographic longitudes reported by the Space Weather Prediction Center (SWPC; Pevtsov 2016) for two active regions, AR 12738 and AR 12839, observed at 00:00 on 2019-110, as well as their locations on the following 2 days. The west-limb location of AR 12738 was near the magnetic footpoints of both *PSP* and *ACE*. By 00:00 on 2019-111, AR 12738 had rotated past the west limb and was no longer visible from Earth. In a companion paper about the events of 2019-110–111, Schwadron et al. (2020) obtain similar results for the footpoint locations and discuss the modeling of the magnetic connection between the photosphere and the source surface.
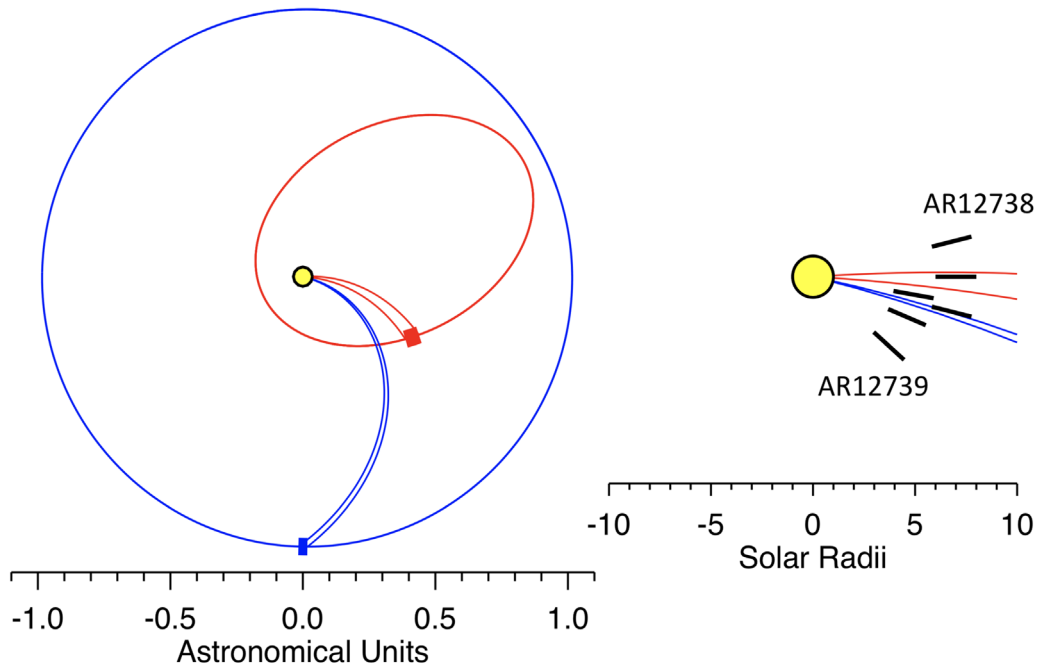
Figure 1. Left: orbits of *ACE* (blue) at Earth and of *PSP* (red) during its second orbit. Thick sections indicate the portions of the orbits traversed between 2019-110 00:00 and 112 00:00. Parker-spiral magnetic field connections to the Sun are shown for these two time limits using measured solar wind speeds of 320 km s^{-1} at *ACE* and 400 km s^{-1} at *PSP*. The Sun is not shown to scale. Right: expanded view close to the Sun. Here, the Sun is shown to scale. Black radial line segments indicate the reported longitudes of AR 12738 and AR 12739 at 00:00 on 2019-110, 111, and 112, reading counterclockwise. Field lines are shown ending at the photosphere. The more complex field between the photosphere and the source surface at which the field becomes radial is not included (see Schwadron et al. 2020).

For operational purposes, the *PSP* mission is divided into "encounter" segments, which are defined as the time between the inbound crossing of 0.25 au and the next outbound crossing of this heliocentric radius. The encounter durations during the first two orbits were approximately 12 days. During encounter, the spacecraft has minimal communication with Earth and stores data on its solid-state recorder (SSR). The time outside of encounter ($r > 0.25$ au) is designated the "cruise" phase. The significance of the encounter/cruise distinction for the present study is twofold. First, the cadence of many of the IS☉IS count-rate measurements is restricted to 1 hr during cruise in order to save most of the data storage for encounter measurements in previously unexplored regions close to the Sun. Second, during cruise there are numerous periods when the spacecraft needs to perform high-speed data downlink to Earth. During these periods, most instruments are turned off to conserve power. As a result, data from energetic particle events that occur during cruise may be fragmentary, or missing entirely.

Thus, as will become clear in the following sections, the data set available from IS☉IS/EPI-Hi during the 2019-110–111 events we are studying, which occurred about 2 weeks after the end of encounter #2, has the limitations of incomplete coverage and low cadence.

3. Instrumentation

3.1. PSP/IS☉IS/EPI-Hi

The EPI-Hi instrument covers the upper portion of the IS☉IS energy range, starting near $\sim$1 MeV nucleon^{-1} for ions and $\sim$0.5 MeV for electrons. It has been described elsewhere by McComas et al. (2016) and Wiedenbeck et al. (2017). Here, we summarize some key features that have direct bearing on the observations we are reporting.

The instrument identifies energetic particles by means of the widely used dE/dx versus total energy technique utilizing measurements of energy losses in a stack of silicon solid-state detectors. For a particle that stops in the detector stack, the energy deposit, E', in the detector where it stopped and the energy loss, ΔE, measured in the immediately preceding detector are used to construct a plot of ΔE versus E'. Signals from different particle species fall in separate regions of such a plot. Boundaries of those regions, which are determined from a combination of calculations and calibrations based on flight data, are used to assign the species of each detected particle.

The IS☉IS/EPI-Hi sensor system contains three cylindrical solid-state silicon detector stacks (called "telescopes"): two low-energy telescopes, designated LET1 and LET2, and one high-energy telescope, designated HET. In the spacecraft's nominal orientation (i.e., near perihelion) the axis of each cylinder lies in the *PSP* orbital plane, with HET and LET1 having their respective sunward apertures (called HET-A and LET-A) oriented 20° and 45° westward of the spacecraft–Sun line and their antisunward apertures (HET-B and LET-B) 200° and 225° westward. Finally, LET2 has its axis perpendicular to that of LET1, and its single aperture (LET-C) is oriented 135° westward of the spacecraft–Sun line. Figure 2 shows drawings of HET and LET1, the two telescopes used in this study. The telescope fields of view are shown in detail by McComas et al. (2016).

In this work, we used electron measurements from the two HET apertures and ion measurements from the two LET1 apertures. Data from LET2 were not used because this telescope, which was designed with a thicker entrance window than LET1 as a precaution against possible high-speed dust impacts, has a higher energy threshold than LET1 and thus recorded significantly fewer energetic ions in the low-intensity, low-energy event we are studying.
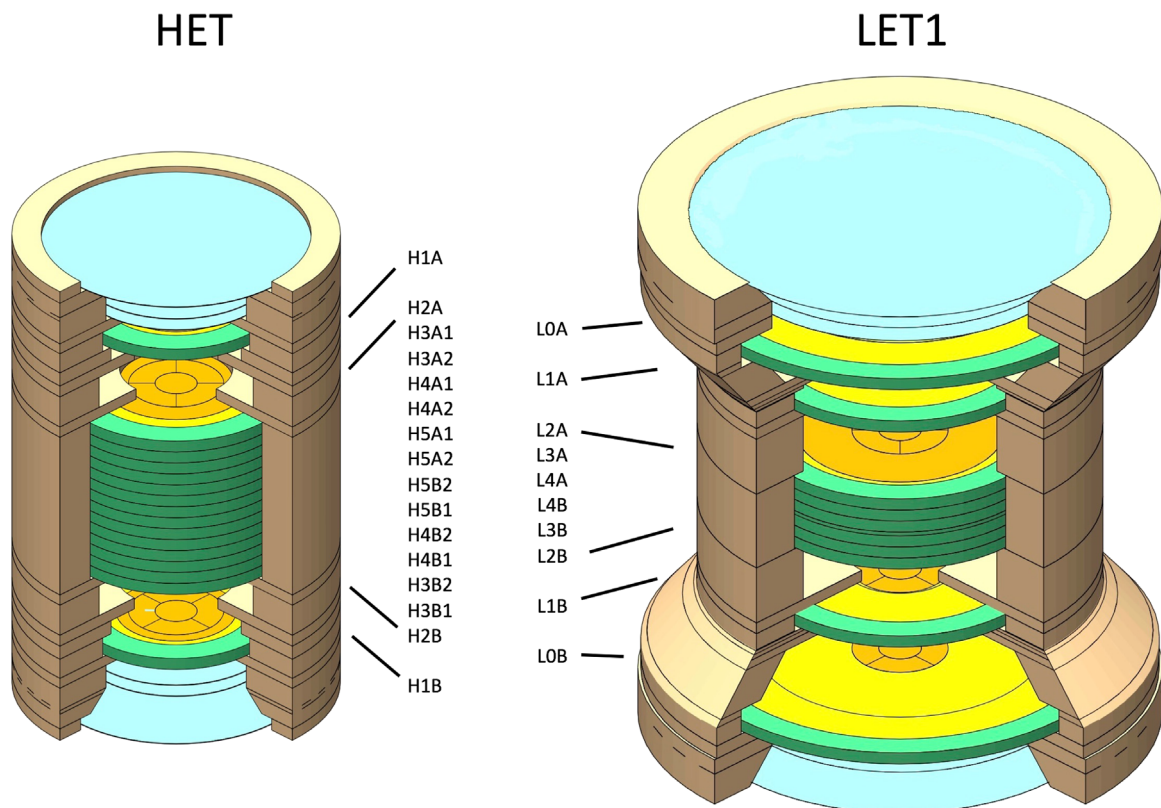
HET   LET1

Figure 2. Illustration of the IS☉IS/EPI-Hi HET and LET1 telescopes. Colors indicate the following: orange–active Si; yellow–inactive Si; green–polyimide detector mounts; blue–Kapton windows; brown/beige–aluminum housing. The two telescopes are shown to the same scale, which can be judged from the thicknesses of the detector mounts (green), each of which is 2.0 mm. Nominal thicknesses of active Si are as follows: L0, 12 μm; L1, 25 μm; L2, 500 μm; L3 and L4, each 1000 μm; H1, 500 μm; H2, 1000 μm; H3 through H5, each 2 × 1000 μm.

The front two detectors in each LET1 aperture are thin, 12 μm followed by 25 μm, and allow ion detections down to ~1 MeV nucleon^{-1} for H and ^{4}He through ~1.5 MeV nucleon^{-1} for Fe (taking into account the three Kapton windows, which together have a silicon-equivalent thickness of ~3 μm). Subsequent detectors, which are significantly thicker and allow ion measurements up to at least 100 MeV nucleon^{-1}, were not used in this study because there were very few ions heavier than He detected beyond the first two detectors.

In IS☉IS/EPI-Hi, the basic data processing needed to derive composition and energy spectra from the detected particle signals is performed on board because the storage on the spacecraft's SSR and the quantity of data that can be transmitted to the ground are both too limited to allow returning all of the raw pulse height measurements. The flight software compares the measured ΔE and E' values with tabulated boundaries for the regions in which each species should fall.

After identifying the detected species, all of the deposited energies from the particle are summed to obtain the total detected energy. To this is added a small correction for the estimated energy loss in the telescope windows. Finally, for ions, the energy per nucleon is calculated by dividing by the mass of the most common isotope of the element. The count of the number of detected particles of each species is maintained in a number of logarithmically spaced E/M bins of width $2^{0.25}$ (approximately 13 bins per decade).

A fraction of the instrument's data storage allocation is used to record and return the raw pulse height measurements from selected samples of events. These samples can be used to check and, if necessary, refine the species boundaries that are stored on board. This is particularly important for events where measurements of ΔE are made in the thinnest detectors (L0 and L1), because these low-energy ions have effective charges that are less than that of the fully stripped nucleus, which affects the range–energy relation needed to calculate the ion species boundaries. During the first two *PSP* orbits, nearly all of the detected heavy nuclei stopped in the first few LET detectors, requiring the use of ΔE measurements from L0 or L1.

The final validation of species boundaries used for identifying heavy elements is awaiting a large-enough SEP event to provide the data needed to precisely establish the locations of the element response tracks. H and He are well separated from other species, and the boundaries calculated before launch are suitable for identifying these elements. The L0, L1, L2, H1, and H2 detectors are segmented to provide information on particle incidence directions (McComas et al. 2016). In order to achieve the mass resolution needed to separate ^{3}He from ^{4}He, we restrict the isotope analysis to He nuclei incident at small angles from the telescope axis, as determined from hits in detector segments that are aligned with one another in L0 and L1.

The partitioning of the He region into subregions suitable for constructing mass histograms also required updating based on flight measurements. The 2019-110–111 period provided the data needed for calibrating the He mass calculation and also improved our understanding of some detector parameters (e.g., dead layer thicknesses). We used this information, together with Geant4 simulations of the instrument response,
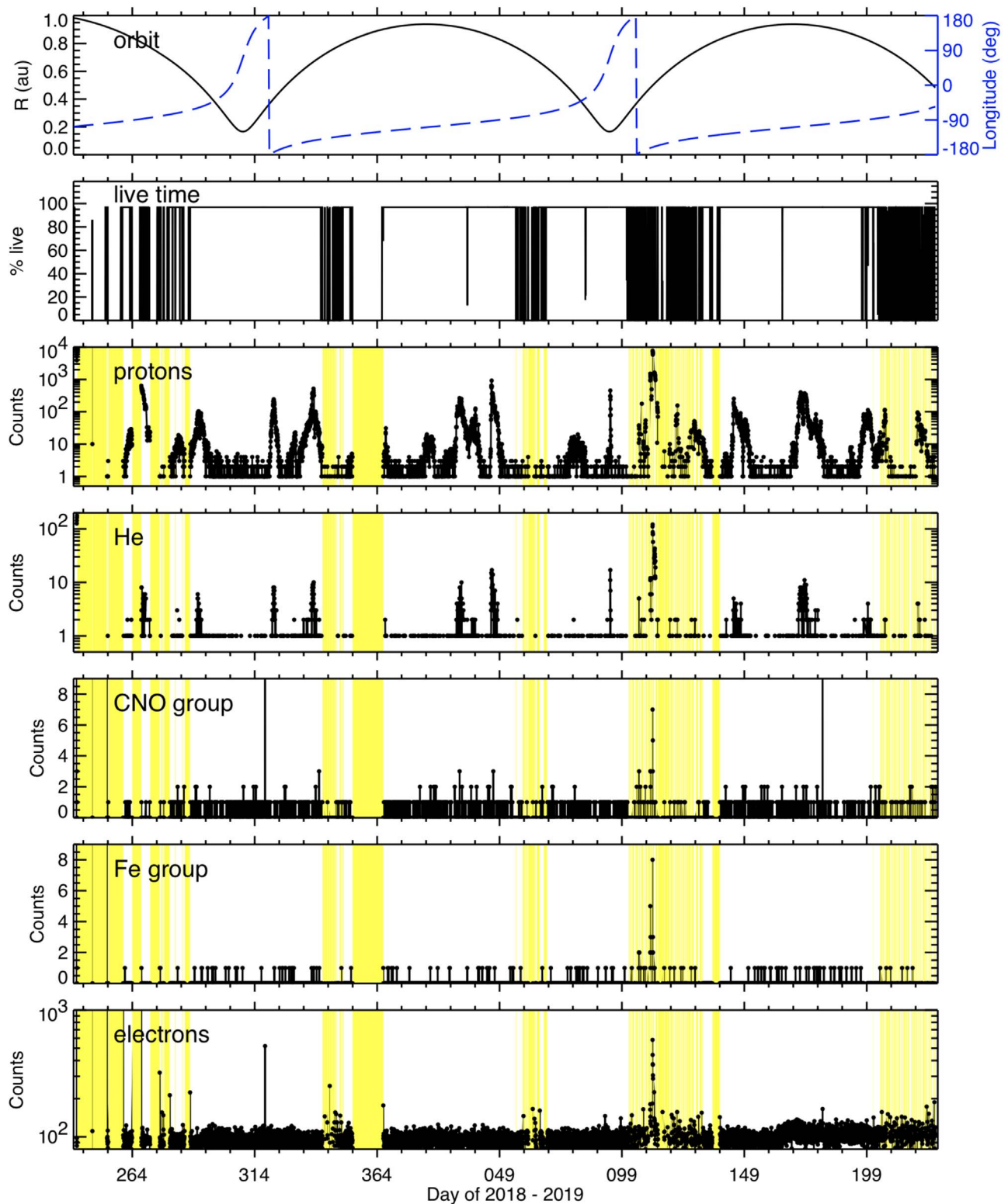
Figure 3. Overview of energetic particle activity at *PSP*. Panel 1 (from top): *PSP* heliocentric radius (solid line) and heliographic inertial (HCI; Thompson 2006) longitude (dashed line). Panel 2: IS☉IS/EPI-Hi fractional live time. Black regions appear when there were many turn-on/turn-off cycles within a short span of time. Panels 3 through 6: sums of hourly count rates from the shortest range of the LET-A and LET-B apertures for protons, He, CNO-group, and Fe-group ions. Note that linear count scales are used for the latter two panels. Panel 7: sums of hourly count rates of electrons from the shortest range of HET-A and HET-B. Yellow vertical bands indicate times when the instrument was not operating. Data points sometimes appear to fall within the yellow region because the instrument on-time was so short that it cannot be distinguished on this timescale. Cohen et al. (2020) discuss the SIR events starting on 2018-287, 320, 332 and 2019-030, 036, 045, 076. Joyce et al. (2020) discuss those starting on 2019-144, 171, and 197. Leske et al. (2020) discuss the SEP event starting on 2019-094. The spike in the electron count rate near 2018-317 is an instrumental artifact.
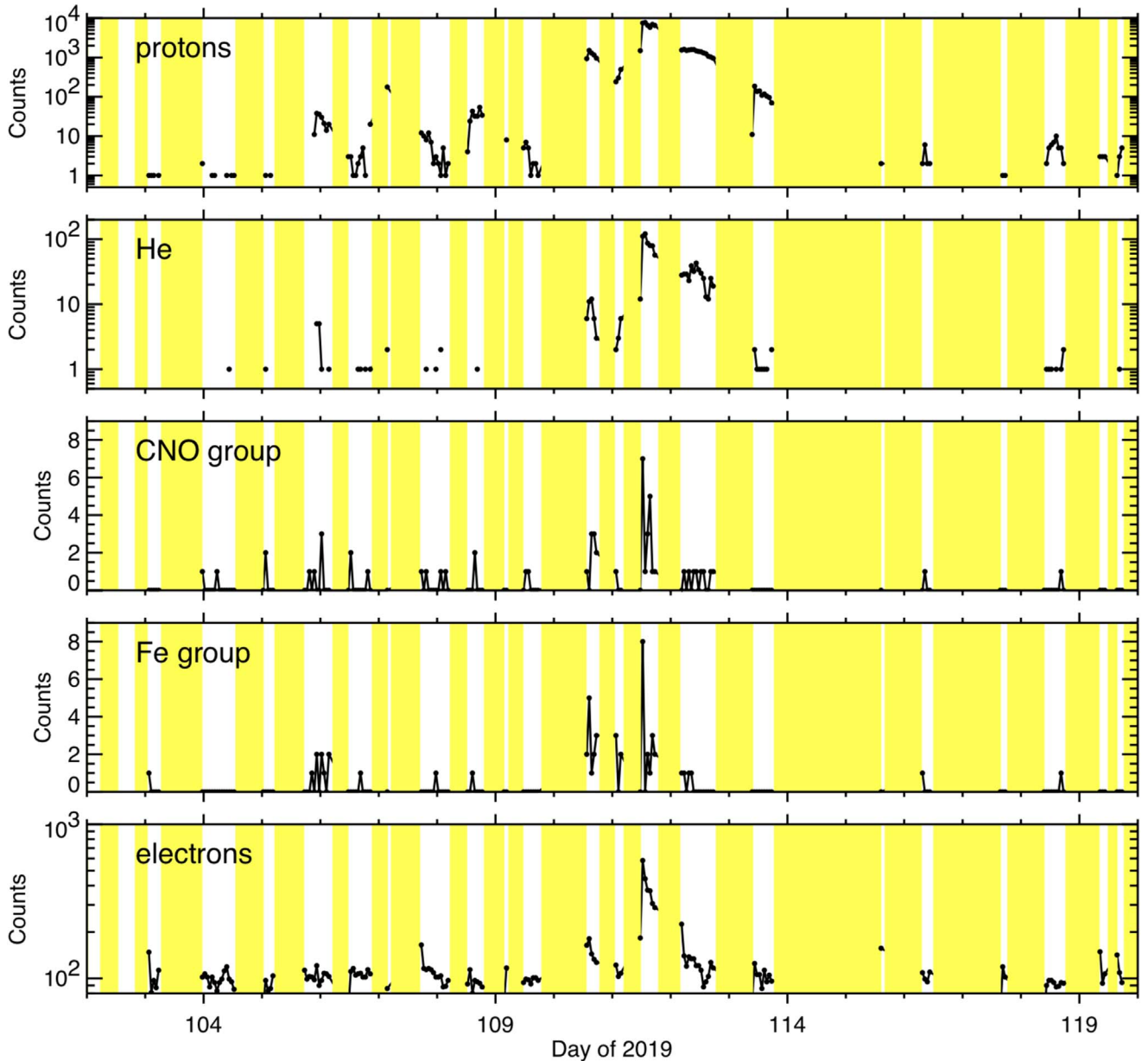
Figure 4. Expanded view of the bottom five panels of Figure 3 around the time of the 2019-110–111 ^{3}He-rich period. The highest intensities observed for each of these five species during the first two *PSP* orbits occurred at this time. Yellow vertical bands indicate times when the IS☉IS/EPI-Hi instrument was turned off, resulting in a "picket fence" through which the energetic particles were observed.

to produce improved species boundaries, which were uploaded to the instrument before the third encounter. In order to analyze heavy-ion elemental composition and He isotopic composition prior to the third encounter, we have relied on the sample of pulse height event data that was returned.

3.2. ACE/Ultra-Low-Energy Isotope Spectrometer (ULEIS)

The ULEIS on *ACE* is a high mass resolution time-of-flight versus total energy spectrometer operating in the energy range from a few tens of keV nucleon^{-1} to a few MeV nucleon^{-1}. It is described in detail by Mason et al. (1998) and has been used for numerous energetic particle studies over the past two solar cycles. It has achieved the best separation of SEP He isotopes of any instrument flown to date.

4. Overview of Energetic Particle Activity

The first IS☉IS observations of the energetic particle environment near the Sun have been summarized by McComas et al. (2019). Figure 3 gives an overview of selected IS☉IS/EPI-Hi measurements from instrument turn-on on 2018 August 29 (2018-241) through shortly before the start of the third solar encounter about 1 yr later. The top panel shows the heliocentric distance of *PSP* (solid line) and its heliographic longitude (dashed line).

The second panel in Figure 3 shows the fraction of time that the IS☉IS/EPI-Hi instrument was "live" for collecting energetic particle data. During this very quiet period, the live-time percentage remained nearly constant at a value greater than 95%. The difference from 100% is due to various housekeeping activities that the instrument must perform. Dips
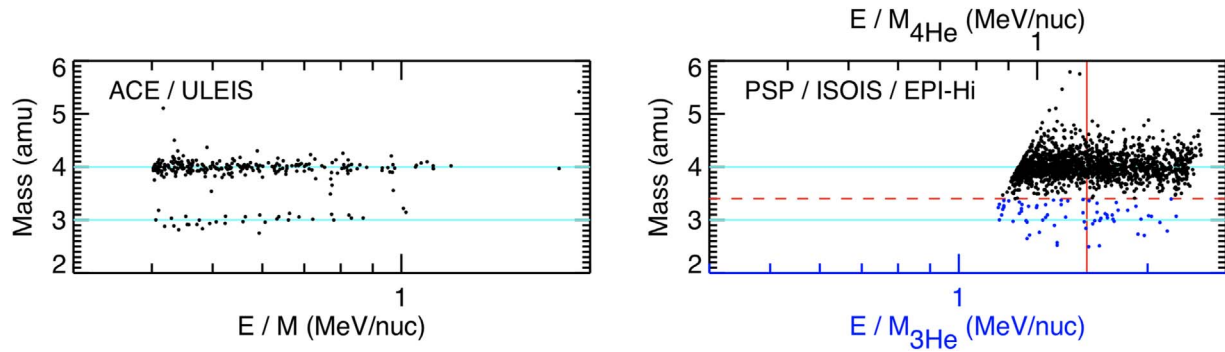
Figure 5. Calculated He mass vs. energy per nucleon for the time period 2019-109 12:00 to 2019-113 12:00. Left: *ACE*/ULEIS He events with 0.4 MeV nucleon^{-1} $\lesssim E/M \lesssim$ 2.0 MeV nucleon^{-1}. Calculation of E/M from time of flight does not depend on mass. Right: *PSP*/IS☉IS/EPI-Hi He events with 0.9 MeV nucleon^{-1} $\lesssim E/M \lesssim$ 1.8 MeV nucleon^{-1} for ^{4}He. Measured total energy is divided by the mass of ^{4}He (black points and upper scale) or the mass of ^{3}He (blue points and lower scale) if the derived mass is greater or less than M = 3.4 amu (dashed red line), respectively.

below the steady, peak value occur when the instrument is turned off, which can happen during periods when increased power is needed for spacecraft operations such as high-speed data downlink. The vertical yellow bands in the bottom five panels of Figure 3 indicate the times when IS☉IS/EPI-Hi was off.

The third through sixth panels from the top show hourly count rates of H (protons), He, CNO-group elements, and Fe-group elements. These are all measured in the shortest range (i.e., stopping in an L1 detector) of the LET1 telescope, combining counts from the LET-A and LET-B apertures. The corresponding energy per nucleon intervals for all of these ion species are similar, with values of $\sim$1–3 MeV nucleon^{-1}. Because of the extremely quiet solar minimum conditions, the total number of detected particles is very low for all of these elements other than H, and even the H rate never exceeded a few counts per second.

Most of the H and He rate increases are attributable to particle acceleration in association with solar wind stream interaction regions (Cohen et al. 2020; Joyce et al. 2020), which are commonly referred to as corotating interaction region events when they are observed more than once near the same Carrington foot-point longitude. Another increase was related to a small SEP event for which there was insufficient information to conclusively establish the acceleration mechanism (2019-094; Leske et al. 2020).

The bottom panel in Figure 3 shows the hourly count rate for electrons in the shortest range (stopping in H2) of the HET telescope, combining counts from the A and B apertures. The only HET detection of count rates exceeding the quasi-steady background of a few hundred counts per hour occurred during the 2019-110–111 interval. Electron count rates in the LET telescopes (not shown) also had significant increases at this time. The origin of the electron background, which we plan to investigate and discuss in a future work, could include Jovian electrons and secondary electrons produced in the spacecraft.

The highest intensities measured for H, He, heavy ions, and electrons all occurred during the events of 2019-110–111, which are the subject of this paper. In subsequent sections, we show that these events exhibit the characteristics of "impulsive" SEP events, in which acceleration is thought to be driven by reconnection in solar flares. In an accompanying paper, Schwadron et al. (2020) argue that CME-driven compressions may have also played a role in compressing and further accelerating these particles.

5. Characteristics of the 2019-110–111 Events

Figure 4 shows the lower five panels of Figure 3 with the timescale narrowed down to a period of 18 days around the time of the 2019-110–111 activity. Although measurements are available less than half of this time (white regions between the yellow bands that indicate off-times), prominent count-rate increases are observed peaking on 2019-111 for all of the species shown. A possible slow increase before this day and a slow decrease afterward are apparent in the proton data, and a suggestion of a similar trend can be seen in some other particle species as well. In the remainder of this section, we discuss the in situ energetic particle observations in the events of 2019-110–111, and in the next section we consider the associated remote sensing observations.

Figure 5 shows calculated mass versus energy per nucleon (E/M) of He nuclei detected by *ACE*/ULEIS and by *PSP*/IS☉IS/EPI-Hi. Here, we have combined data from a 4-day period extending from 2019-109 12:00 to 2019-113 12:00. In this figure, each dot represents an individual detected particle. As shown below (Figure 7), nearly all of the He particles were actually collected on 2019-110–112, both at *PSP* and at *ACE*.

For IS☉IS/EPI-Hi, using the pulse height event data, we selected the He nuclei that stopped in the L1 detector of either the LET-A or the LET-B aperture (Figure 2). Combining the energy loss in the L0 detector (ΔE) with the residual energy measured in the L1 detector (E'), we calculated the mass of each detected He particle. Adding these two signals, we obtained the total measured energy and applied a small correction for the energy lost in the telescope windows. It is conventional to compare abundances at equal energy per nucleon values, which corresponds to equal velocity. The right panel in Figure 5 shows E/M values obtained assuming the ^{4}He mass (upper horizontal scale) and assuming the ^{3}He mass (lower scale). Since the ^{4}He mass distribution can have low-side tails that extend into the ^{3}He region, there can be some ambiguity about what mass should be used for calculating E/M for individual particles. We have adopted a cut at M = 3.4 amu (red dashed line) to separate the two isotopes. Corrections can be made on a statistical basis to account for spillover.

The overall width of the ^{4}He mass distribution increases toward lower energies owing primarily to the effects of multiple Coulomb scattering and energy-loss fluctuations in the ΔE detector. One can select the higher-energy portion of the distribution to obtain a subset of the data that has better mass separation. We have used a cut at an E/M_{4He} value of

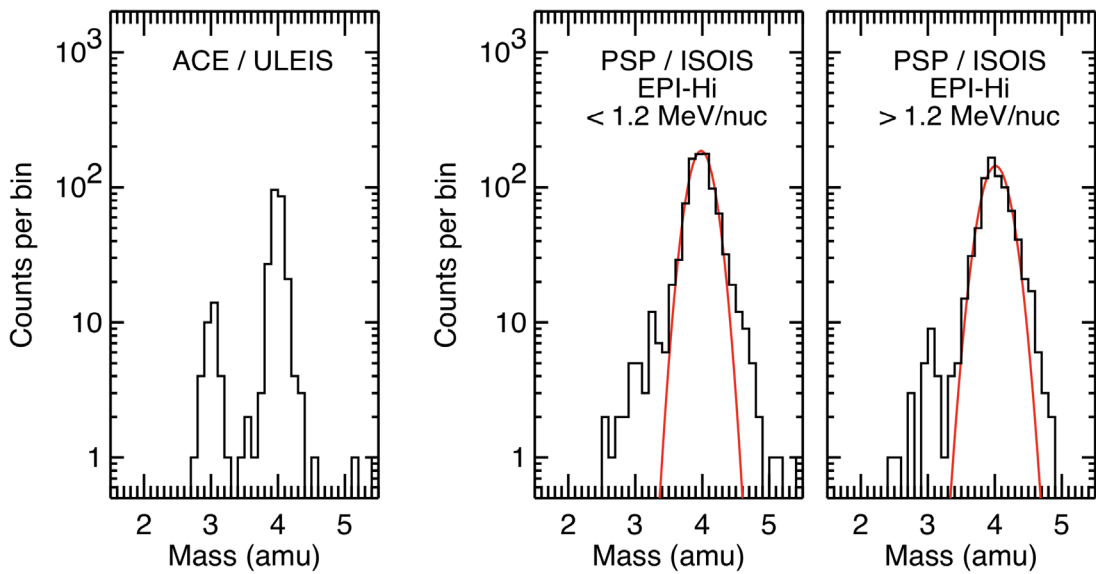**Figure 6.** Mass histograms for the time period 2019-109 12:00 to 2019-113 12:00 from *ACE*/ULEIS and IS⊙IS/EPI-Hi. The IS⊙IS/EPI-Hi histograms are shown for two subsets of the data selected based on whether the E/M value is less than or greater than 1.2 MeV nucleon^{-1}, where E/M is calculated from the total energy and the assumption that $M = 4$. Red curves show Gaussian fits to the central regions of the ^{4}He peaks in the two IS⊙IS/EPI-Hi panels.
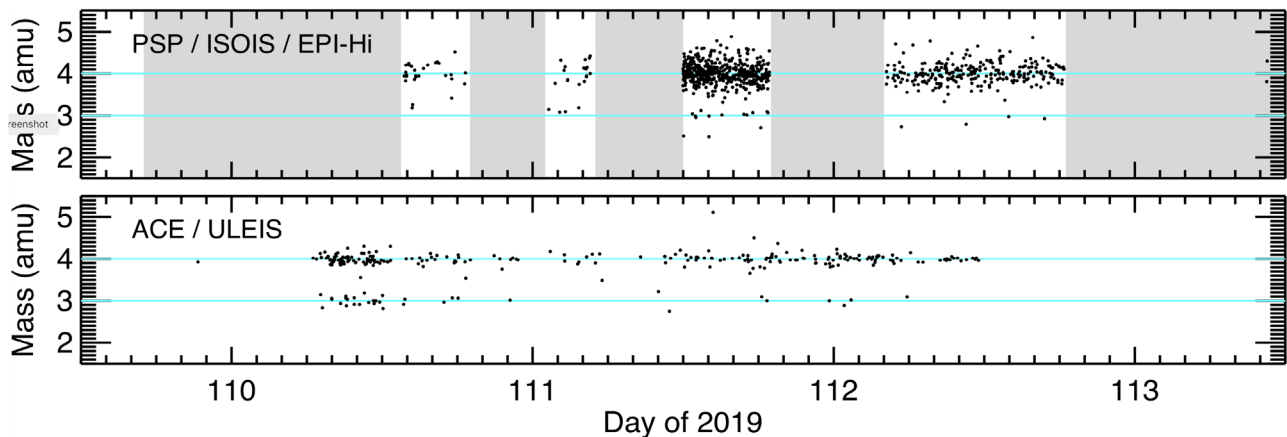

Figure 7. Calculated He mass vs. time from *PSP*/IS⊙IS/EPI-Hi and *ACE*/ULEIS. The IS⊙IS/EPI-Hi data are restricted to events from the >1.2 MeV nucleon^{-1} subset shown in the right panel of Figure 6. Gray regions indicate times when IS⊙IS/EPI-Hi was turned off.

1.2 MeV nucleon^{-1} (corresponding to 1.6 MeV nucleon^{-1} for the ^{3}He particles), which is indicated by the vertical red line in Figure 5. The diagonal left and right edges of the distribution correspond to the points at which particles just enter and exit the E' detector, L1, and are caused by anticorrelated variations of ΔE and E', which can occur as a result of variations in the particle path lengths through the ΔE detector (e.g., caused by differences in incidence angle) or Bohr/Landau fluctuations in ΔE. Simulations of the instrument response can be used to take these effects into account. Particles with E/M values beyond the high-energy end of the distribution are detected and identified using detectors deeper in the telescope. The relatively small number of He nuclei reaching the L2 detector in this weak event were not used in this study.

Figure 6 shows mass histograms that result from projecting the data shown in Figure 5 on the mass axis. The middle panel corresponds to the region of the IS⊙IS/EPI-Hi plot to the left of the vertical red line and the right panel to the region to the right of this line. The red curves show Gaussian fits to the central regions of the ^{4}He peaks, which result in similar

standard deviations of $\sigma_M = 0.18$ and 0.20 amu for the low- and high-E/M regions, respectively. However, the low-energy mass peak has more prominent non-Gaussian tails.

Figure 7 shows the derived masses of the detected He events as a function of the time of detection at both *PSP*/IS⊙IS/EPI-Hi (top panel) and *ACE*/ULEIS (bottom panel). In order to obtain good separation between ^{3}He and ^{4}He, only those He events from *PSP*/IS⊙IS/EPI-Hi that have $E/M_{^4\mathrm{He}} > 1.2$ MeV nucleon^{-1} were used. *ACE*/ULEIS measured the highest intensity of both He isotopes on 2019-110 before midday. This was during one of the intervals during which IS⊙IS/EPI-Hi was turned off (gray bands). After midday on 2019-111, when IS⊙IS/EPI-Hi observed the highest intensity of both isotopes, *ACE*/ULEIS was still observing ^{3}He, but intensities of both He isotopes were lower than they had been during the first half of the previous day. The event at *PSP*/IS⊙IS/EPI-Hi continued through much of 2019-112, being cut off when the instrument was again turned off around 18:30 on 2019-112. At *ACE*/ULEIS, no He was observed after midday on 2019-112.
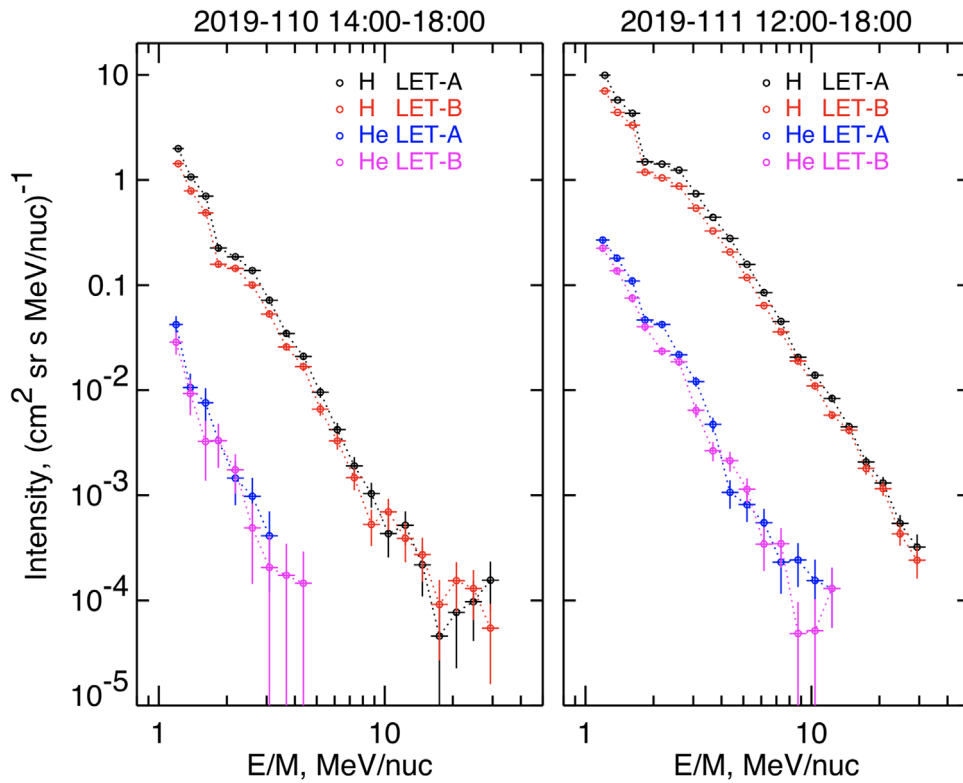
Figure 8. H and He energy spectra from the LET-A and LET-B apertures for the indicated time periods on 2019-110 (left) and 111 (right). The dip in the intensities near ~2 MeV nucleon^{-1} is an uncorrected instrumental effect associated with the transition from stopping in the L1 detector to stopping in L2. Flattening due to contributions from cosmic-ray backgrounds occurs at the highest energies.

To derive abundance ratios between ^{3}He and ^{4}He, we have used IS⊙IS/EPI-Hi data from the E/M interval 1.35–1.75 MeV nucleon^{-1}, over which both He isotopes stop in the L1 detectors (Figure 5). For the time period during which IS⊙IS/EPI-Hi has the highest statistics, 12:00–19:00 on 2019-111, we obtained the ratio ^{3}He/^{4}He = 0.063 ± 0.016. The data are statistically very limited when restricted to these relatively narrow energy and time intervals, which is reflected in the quoted uncertainty.

During this same time interval, the IS⊙IS/EPI-Lo instrument (McComas et al. 2016; Hill et al. 2017) observed a measurable intensity of ^{3}He below 1 MeV nucleon^{-1}. Preliminary analysis indicates a ^{3}He/^{4}He ratio within a factor of two of the IS⊙IS/EPI-Hi value given above.

From *ACE*/ULEIS data in the energy range 0.5–2.0 MeV nucleon^{-1}, we find a ^{3}He/^{4}He ratio of 0.21 ± 0.08 for the time interval 00:02-12:00 on 2019-110 and 0.087 ± 0.030 for the 2-day period covering 2019-111 and 112. It is not surprising that there can be differences among the ^{3}He/^{4}He ratio values, given that there are differences in the times, locations, and energies of the various measurements.

Figure 8 shows measured energy spectra for H and He during time intervals on 2019-110 (left) and 111 (right). Spectra are shown separately for particles that entered the LET-A aperture and particles traveling in the opposite direction that entered the LET-B aperture. Comparison of the spectra from the two apertures shows that the particle distributions were close to isotropic at this time. The differences between the intensities measured by LET-A and LET-B are small enough that we cannot yet rule out the possibility that they could have an instrumental origin. For example, small portions of the two

fields of view are obstructed by different parts of the spacecraft, which has not yet been taken into account in our calculated geometrical factors. In addition, Compton–Getting corrections (e.g., Ruffolo et al. 1998) have not yet been applied. This effect tends to increase the intensity measured in the sunward-viewing LET-A aperture relative to that measured in the antisunward-viewing LET-B, so the correction would cause a small reduction in the LET-A/LET-B ratio seen in Figure 8. Fits to the measured spectra give power-law indices of −3.6 and ~−4.8 for H and He, respectively, in the 2019-110 event. In the 2019-111 event, the corresponding values were −2.8 and −3.6. For comparison, Leske et al. (2020) report a value of −4.36 for the H spectrum in the SEP event of 2019-094.

The lower limit of the He energy coverage in IS⊙IS/EPI-Hi is within a factor of ~2 of the upper limit in *ACE*/ULEIS. Extrapolating the IS⊙IS/EPI-Hi He intensity from 2019-110 down to 1 MeV nucleon^{-1}, we find ~0.1 cm^{-2} s^{-1} sr^{-1} (MeV nucleon^{-1})$^{-1}$ (within a factor of ~2). Converting the He fluence spectrum obtained by ULEIS over the time interval 00:02 to 12:00 on 2019-110 to average intensity, we find ~0.025 cm^{-2} s^{-1} sr^{-1} (MeV nucleon^{-1})$^{-1}$. It is interesting that the intensity ratio ~4 is similar to the $1/r^2$ ratio that one might expect just based on geometry and the fact that *PSP* was a factor of ~2 closer to the Sun than *ACE*. However, the fact that the ULEIS data were collected during the first half of the day (when IS⊙IS was turned off) and the IS⊙IS/EPI-Hi data were collected during the second half suggests that this comparison might not be significant. Furthermore, the ULEIS counts shown in Figure 7 suggest a drop in intensity around midday on 2019-110, leaving open the possibility that different particle injections were being observed before and after that time.

Figure 7 also shows that during the second half of 2019-111, when IS☉IS/EPI-Hi was seeing its highest ^{4}He count rates, *ACE*/ULEIS rates were lower than those recorded on 2019-110. Some differences are to be expected owing to different connections to the source (Figure 1) and to time–intensity profiles that may be shifted in time and/or have a significant radial variation in intensity. The gaps in the IS☉IS data set prevent us from conclusively determining the cause. It is hoped that future observations of ^{3}He-rich events at *PSP* and *ACE* or *STEREO-A* will provide a clearer picture of how the particle intensities vary with heliocentric radius, longitudinal separation, and energy.

As illustrated in panels 3 and 4 of Figure 4, the numbers of detected nuclei heavier than He are very low. However, it is evident that the numbers of detected particles from the CNO group and from the Fe group are comparable. This observation, taken together with the fact that the E/M intervals for O and Fe particles stopping in the L1 detector are similar, indicates an Fe/O ratio more like the value ∼1 typically found in ^{3}He-rich events than like the values ∼0.04–0.14 characteristic of the solar wind and gradual SEP events (Reames 2018). The *ACE*/ULEIS energy spectra from 2019-110 00:02-12:00 indicate an Fe/O ratio between ∼1 and ∼2.5 for energies in the range of 0.5–1.5 MeV nucleon^{-1}.

As noted above, a common feature of impulsive SEPs is an association with energetic electron events. As shown in the bottom panels of Figures 3 and 4, IS☉IS/EPI-Hi observed a significant increase in the count rate of electrons with energies around an MeV on 2019-111. On 2019-110, there is also an indication of a minor increase in the electron rate. The highest rate measured that day was about a factor of three less than on the following day and only about a factor of two greater than the background. These electron rate increases can be compared with electron measurements at energies below 200 keV made at *ACE*, where the Electron, Proton, and Alpha Monitor (EPAM) instrument (Gold et al. 1998) observed two electron events on 2019-110 with onsets at ∼01:13 and ∼09:40 and one on 2019-111 starting at ∼05:07, as shown in Figure 9. These events are discussed in greater detail by Schwadron et al. (2020). Direct comparison of electron intensities at *ACE* and *PSP* is hindered by the fact that IS☉IS/EPI-Hi was turned on nearly 12 hr after the onset of the first electron event at *ACE*/EPAM on 2019-110 and more than 6 hr after the onset on 2019-111. Thus, the IS☉IS/EPI-Hi detections occurred well into the decay phases of both of these events.

Figure 10 is a plot of $1/v$ versus time of detection for particles collected by *ACE*/ULEIS. Drawing a straight line through the onset times (dashed red line on the plot) yields the time at which the ions were released from the Sun, $t_0 \simeq 01:08$ (± 15 minutes) on 2019-110, and the distance traveled by the first-arriving particles, $L \simeq 1.59$ ($+0.11$, -0.07) au. These approximate uncertainties were estimated using graphical techniques. This ion release time and the release time for the first electron event (Figure 9) are similar and do not show the ∼1 hr delay from the electron release to the ion release that was found by Wang et al. (2016) in a sample of 10 electron/^{3}He-rich SEP events. However, the delays derived in that study are somewhat uncertain because limited counting statistics did not allow derivation of precise path lengths and nominal values of 1.2 au were assumed. A long path length, such as the 1.59 au found in the 2019-110 event, would cause an overestimate of the ion release time delays. IS☉IS/EPI-Hi was turned off at the
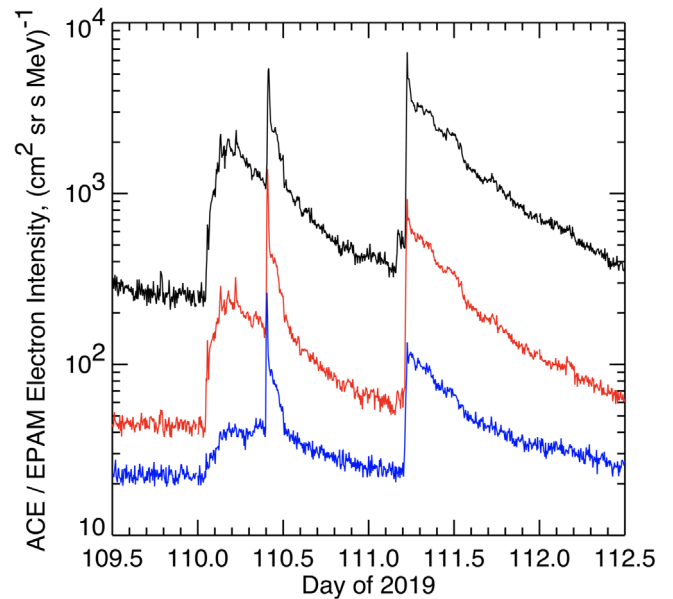
Figure 9. *ACE*/EPAM 5-minute average electron intensities vs. time in three Low Energy Foil Spectrometer (LEFS) energy channels: black–LEFS60/E1′, ∼53 keV; red–LEFS60/E2′, ∼79 keV; blue–LEFS60/E3′, ∼133 keV.
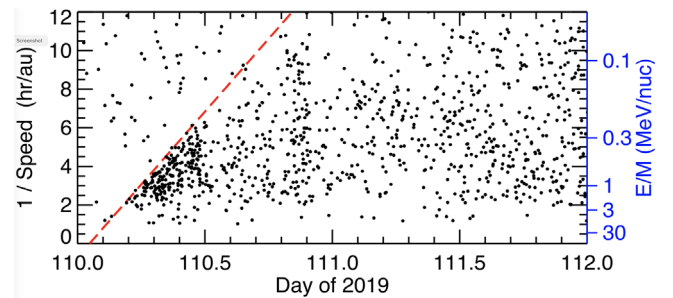
Figure 10. *ACE*/ULEIS $1/v$ vs. time plot for 2019-110 through 111, including ions with masses in the range of 10–70 amu. The scale at the far right in blue indicates E/M values corresponding to selected $1/v$ values. The dashed red line indicates the energy dependence of the event onset time at *ACE*. This line corresponds to an onset at high energy at 01:08 on 2019-110 and a path length of 1.59 au traversed between the source and the spacecraft. For the 2019-111 event, ULEIS did not observe a sharp onset.

times that the 2019-110 electron and ion onsets would have been expected and thus did not provide additional information about the particles' release or about the distance traveled from the Sun to *PSP*.

6. Remote Sensing Observations

As context for our discussion of remote sensing observations, Figure 1 shows the locations of *PSP* and *ACE* (near Earth), their magnetic footpoints, and active regions reported for 00:00 on 2019-110, 111, and 112. At 00:39 on 2019-110, *GOES* observed the onset of a B8.1 X-ray flare (Figure 11, lower left) from an active region (AR 12738) on the west limb of the Sun, and the Atmospheric Imaging Assembly instrument (AIA; Lemen et al. 2012) on the *Solar Dynamics Observatory* (*SDO*; Pesnell et al. 2012) imaged the onset of a jet from the same region. The top left panel of Figure 11 shows the jet 7 minutes later. The video from which this image was taken shows a clear helical twisting motion of the outflowing jet
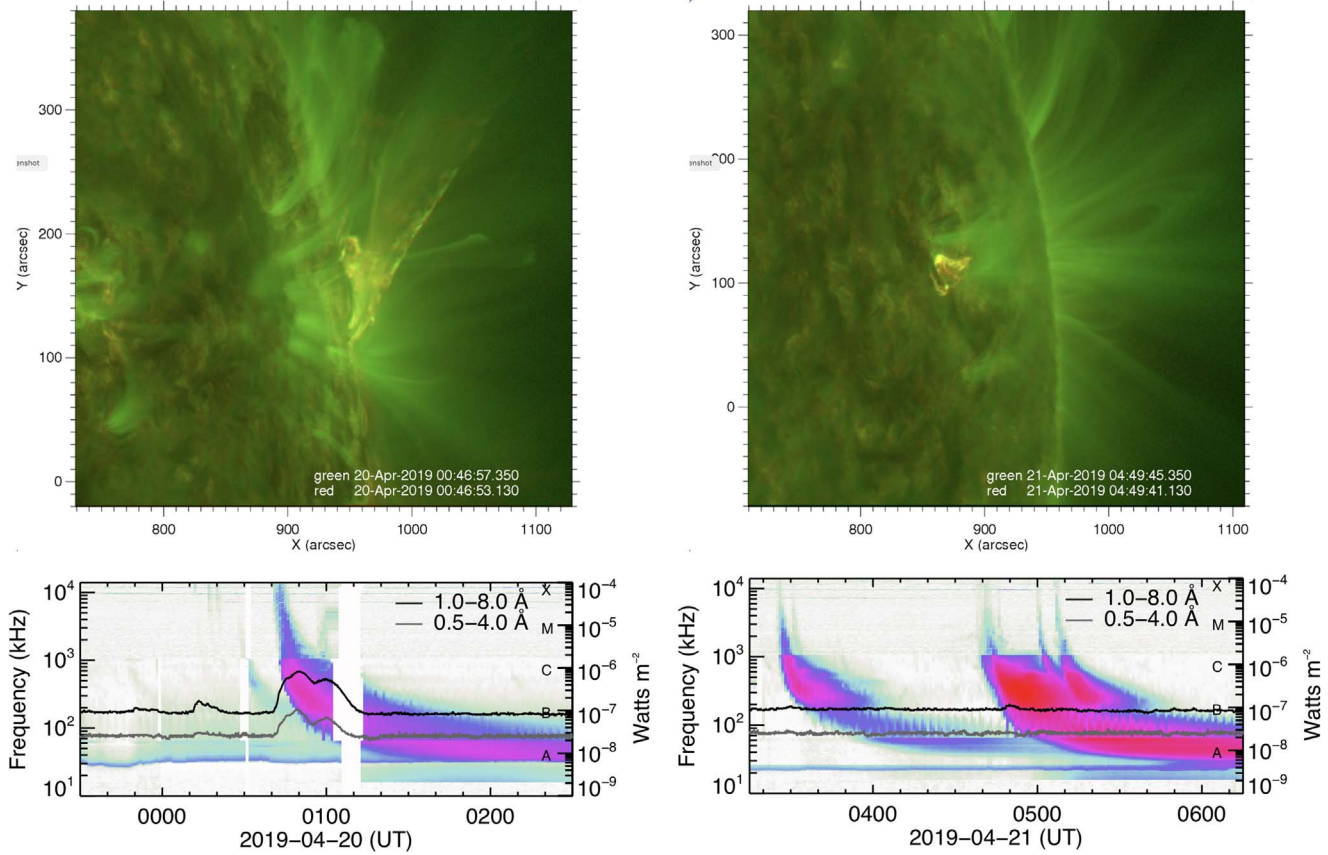
Figure 11. Remote sensing observations of jets (top panels) and of solar X-rays and type III bursts (bottom panels). Jet observations are from *SDO*/AIA, X-ray observations from *GOES*, and type III observations from *Wind*/WAVES. An animation of the jet images is available. The first 4 s of the video shows the 20-Apr-2019 jet. This sequence begins at approximately 00:35 and runs to about 00:55. The 2019 April 21 jet is displayed in the last 5 s. It begins around 04:40 and goes to 05:05. The full real-time duration of the video is 9 s.

(An animation of this figure is available.)

material. Bučík et al. (2018) have previously shown examples of this type of motion in jets associated with ³He-rich events. Type III radio emission was observed by the *Wind*/WAVES instrument starting at 00:42 (Figure 11, bottom left panel). The *PSP*/FIELDS Radio Frequency Spectrometer (RFS) instrument (Bale et al. 2016) also makes solar radio burst measurements, but this emission occurred during a *PSP*/FIELDS data gap.

On 2019-111, AR 12738 was beyond the west limb and no longer visible from Earth. Thus, flares or jets from this region would have been obscured. There was a second active region, AR 12739, not too far from the west limb on 2019-111. No X-ray events were reported from this region, but a jet onset was observed by *SDO*/AIA around 04:45 (Figure 11, top right panel). At that time, AR 12739 was located near N05W70. Type III radio bursts were observed by *Wind*/WAVES on 2019-111 between 03:20 and 05:10 (bottom right panel). *PSP*/FIELDS radio data clearly show the burst starting around 03:26, but the instrument was turned off around 04:30 and missed the later bursts. Since the bursts seen by *Wind*/WAVES around and after 04:40 appear obscured (Figure 11, bottom right panel) at high frequencies (i.e., low in the corona), they probably originated from AR 12738, slightly beyond the limb.

7. Discussion

Figure 12 combines the in situ and remote sensing observations on a common timescale to facilitate the

understanding of interrelationships among the various data. Early on 2019-110, *SDO*/AIA observed a narrow, helical jet from AR 12738 (panel (a)), an associated *GOES* X-ray event (panel (b)), and a *Wind*/WAVES type III radio burst starting at high frequency (panel (c)). Shortly thereafter, *ACE*/EPAM observed the onset of a near-relativistic electron event (panel (d)). *ACE*/ULEIS observed the onset of an event in ~1 MeV nucleon⁻¹ ions about 4 hr later (panel (f)). The ion event had a clear velocity dispersion (panel (e)) that could be extrapolated to $v = \infty$ to obtain the release time from the Sun (panel (e) and Figure 10), which was consistent with the release time derived from the EPAM electron measurements. Resolved measurements of ³He and ⁴He were obtained from both *ACE*/ULEIS near Earth (panel (g)) and *PSP*/IS☉IS/EPI-Hi near 0.46 au (panel (h)). The measurements at *PSP* started about half a day after onset of the event at the Sun when IS☉IS/EPI-Hi was turned on; IS☉IS/EPI-Hi had been turned off to save power while the spacecraft was downlinking data. IS☉IS/EPI-Hi was turned on and off several more times during the following days.

A second solar event, for which there was a jet detection at the west limb (probably from AR 12738) by *SDO*/AIA and which was accompanied by *GOES* X-rays and EPAM electrons, occurred between 09:00 and 10:00, but no sharp ion onset was detectable at *ACE*/ULEIS. A small event at this time could have added into the ongoing ion signals from the earlier event and gone undetected. When IS☉IS/EPI-Hi was
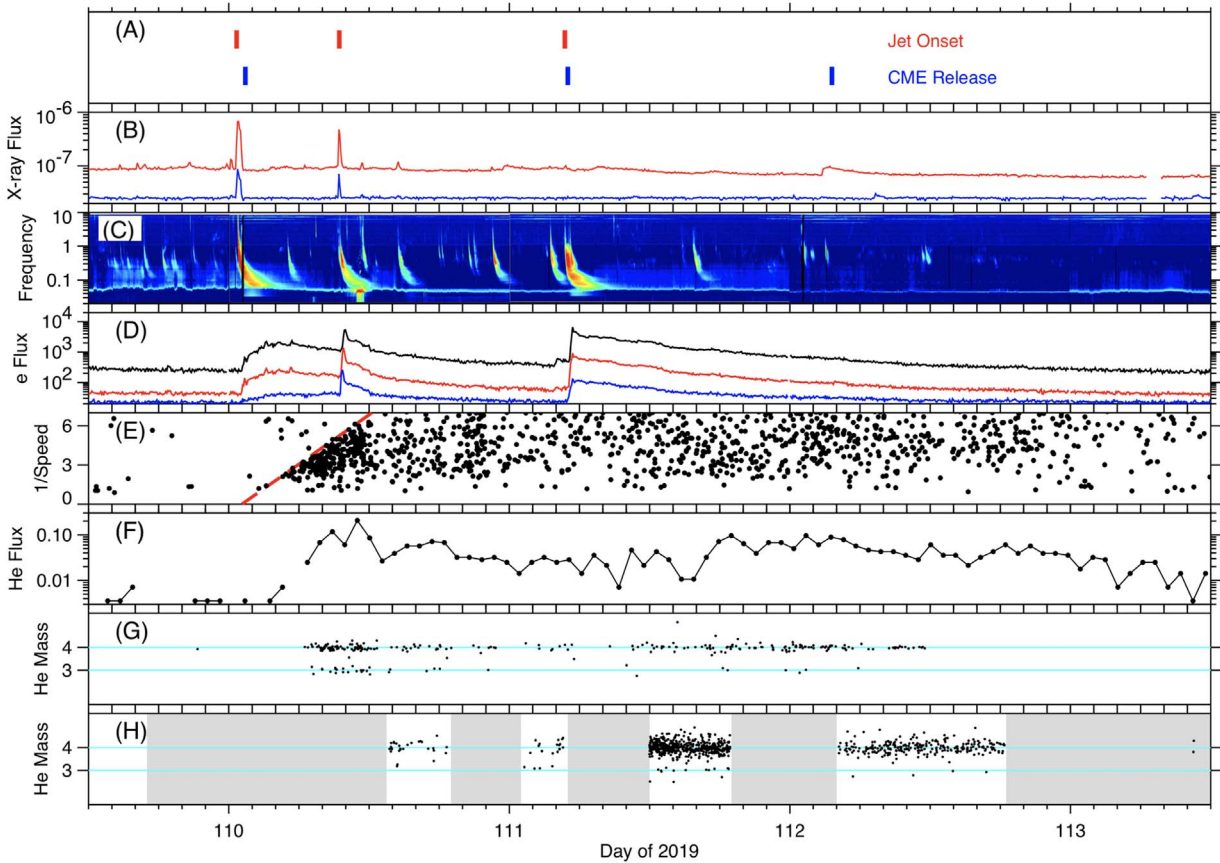
Figure 12. Timing comparison between in situ and remote sensing observations. (a) Onset times of jets (Figure 11) and release times of CMEs reported by Schwadron et al. (2020); (b) *GOES* 5-minute average X-ray flux in the wavelength bands of 0.05–0.4 nm (blue) and 0.1–0.8 nm (red); (c) *Wind*/WAVES dynamic radio spectra; (d) *ACE*/EPAM electron fluxes at ~53, 79, and 133 keV (Figure 9); (e) *ACE*/ULEIS velocity dispersion ($1/v$ vs. time) from Figure 10; (f) *ACE*/ULEIS flux of He (^{4}He+^{3}He) at ~1 MeV nucleon^{-1}; (g) *ACE*/ULEIS He mass vs. time (Figure 7); (h) *PSP*/IS☉IS/EPI-Hi He mass vs. time (Figure 7). Units for the vertical scales in the lower seven panels are (b) W/m^2; (c) MHz; (d) cm^{-2} sr^{-1} s^{-1}MeV^{-1}; (e) hr au^{-1}; (f) cm^{-2} sr^{-1} s^{-1} (MeV nucleon^{-1})$^{-1}$; (g and h) amu. Times shown are at the observer. Travel times from the Sun are approximately ~8 minutes for photons, ~1/2 hr for 80 keV electrons traveling 1.59 au, and ~5 hr for 1 MeV nucleon^{-1} ions traveling 1.59 au.

turned on around 13:00, a relatively weak signal was detected in He and also in electrons (Figure 4).

Shortly before 05:00 on 2019-111, *SDO*/AIA imaged a jet from AR 12739 (Figure 11, top right panel), but with no accompanying X-rays. *Wind*/WAVES did observe type III radio emission at this time (bottom right panel), but the high-frequency portion of the burst was very weak. We attribute the lack of an X-ray detection and the weakness of high-frequency type III emission to an origin at AR 12738, which was behind the limb and obscured when viewed from Earth. The occurrence of a jet from AR 12739 close to the time of the X-ray event at AR 12738 may simply have been a chance coincidence. Alternatively, one can speculate that the flare-related change in the magnetic fields near AR 12738 may have caused a change near AR 12739 that might have been sufficient to trigger the jet.

On 2019-111, *ACE*/EPAM did detect a near-relativistic electron event and *ACE*/ULEIS observed an increase in the detection rate of ^{4}He after 10:00. The highest He isotope count rates observed by *PSP*/IS☉IS/EPI-Hi during the 4-day period shown in Figure 12 were present when the instrument turned on around 12:00 and persisted into 2019-112, with some additional off-times. The SEPs measured by IS☉IS/EPI-Hi on 2019-111 had the highest intensities of H, He, heavy ions, and

electrons observed up to that time in the *PSP* mission (Figure 4), although the absolute intensities were small compared to many events that have been observed near Earth during more active times in earlier solar cycles. Little or no anisotropy was observed in the H and He intensities measured in IS☉IS/EPI-Hi's LET1 telescope, although we cannot rule out a strong anisotropy near the beginning of the event, hours before the start of the IS☉IS/EPI-Hi observations.

Several CMEs were observed during the time period shown (panel (a)). Schwadron et al. (2020) reported that an interplanetary coronal mass ejection (ICME) associated with the CME that was imaged on 2019-110 arrived near *PSP* the following day and may have been responsible for a modest reacceleration of the particles from the impulsive event of 2019-111.

In order to further test our conclusion that AR 12738 must have been the source of the SEP event observed on 2019-111, as well as that observed the previous day, we have looked into the activity reported from all of the active regions listed in the SWPC's event reports between 2018 mid-November and 2019 mid-June. Figure 13 is a plot of the Carrington latitude (top panel) and Carrington longitude (bottom panel) for each active region as a function of time. Superimposed on the short curves indicating the active regions, ⊕ symbols are plotted at
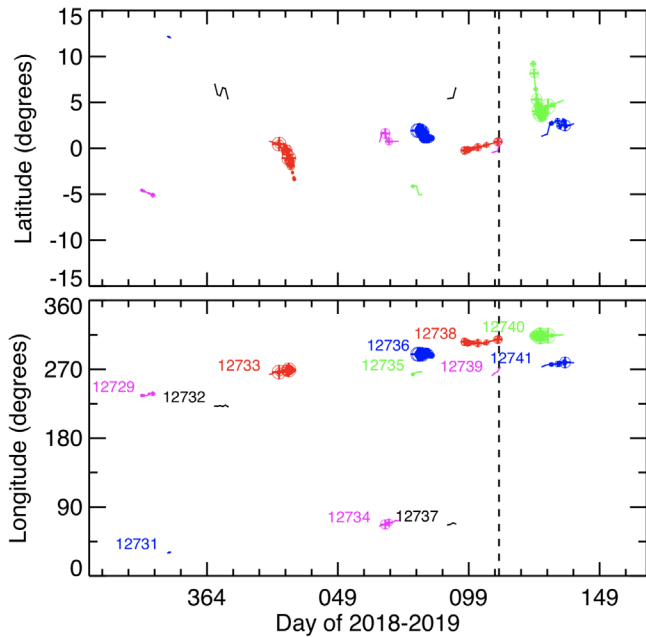
Figure 13. Carrington latitude (top panel) and longitude (bottom panel) at which X-ray flare detections from *GOES* were reported by the SWPC between 2018-319 and 2019-166 (2018 mid-November to 2019 mid-June). Active regions are indicated by color and labeled in the bottom panel. Times of flares associated with each region are shown with $\oplus$ symbols, with larger symbols corresponding to higher peak X-ray fluxes. The dashed vertical line indicates a time between the two ^{3}He-rich SEP events reported in this paper.

the time of each reported X-ray flare from each region, with larger symbols indicating higher peak X-ray fluxes. Different colors are used to distinguish active regions, with the region numbers indicated in the bottom panel. Because magnetograms and X-ray event observations are only available from Earth, the duration of each sequence of observations of a given active region and its X-ray activity is limited to the ∼2 weeks when the region is on the Earth-facing hemisphere of the Sun.

From this presentation using Carrington coordinates, it is evident that there were only a few genuinely distinct active regions on the Sun during this 7-month period. SWPC regions numbered 12729, 12733, 12736, 12738, and 12740 were, in actuality, all appearances of region 12738, which we have been discussing. Similarly, 12732, 12735, 12739, and 12741 apparently coincide, as do 12734, 12737, and possibly 12731. Clearly, there are time intervals, sometimes extending over several solar rotations, during which there are no reports of active regions related to one or more of these groupings (e.g., between ∼2019-035 and ∼2019-060). However, examination of magnetograph images shows that clusters of both field polarities were still present around the same Carrington longitude.

It is very likely that the ^{3}He-rich SEP event of 2019-111 (as well as that of 2019-110) was produced by AR 12738, given that this region and related active regions at the same Carrington coordinates were repeatedly producing X-ray flares while AR 12739 produced very few until it finally became more active (under the name AR 12741) around 2019-130.

Not only did AR 12738 produce numerous X-ray flares, but it was also the source of other SEP events. E. C. Roelof et al. (2020, in preparation) discuss one of these, which was detected by IS⊙IS/EPI-Hi on 2019-092 when *PSP* was very close to its second perihelion. This event contained sizable enhancements of heavy elements, which provides an indication that it was impulsive, even though ^{3}He was not observed. Leske et al. (2020) discuss a small, highly anisotropic SEP event from AR 12738 that occurred 2 days later, on 2019-094. Examining He mass spectrograms from *ACE*/ULEIS, we found another, somewhat smaller, ^{3}He-rich SEP event from AR 12736 (the immediate predecessor to AR 12738) on 2019-080, just one solar rotation before the events of 2019-110–111.

Comparisons of the characteristics of impulsive SEP events observed at *PSP* and near Earth are of interest because of the information they can provide about how these characteristics are affected by transport processes. On strictly geometric grounds, it can be argued that energetic particle fluences in ^{3}He-rich events should vary approximately as $1/r^2$ with the distance, r, of the observer from the Sun. Peak particle intensities may have a stronger variation, possibly as strong as $1/r^3$, because particles from an abrupt, point injection at the Sun undergo velocity dispersion and pitch-angle scattering (a portion of which may be compensated by adiabatic focusing) and become more spread out in time at larger distances from the Sun.

Earlier studies (Mason et al. 1989; Wibberenz & Cane 2006) combining data from the *Helios* spacecraft, which had perihelion distances of ∼0.3 au, and near-Earth spacecraft reported a few ^{3}He-rich SEP events that were detected at both locations and were found to have much faster rise times and much higher peak intensities close to the Sun.

The comparison of the measurements at *PSP* and *ACE* for the events of 2019-110–111 does not provide strong indications that the event onsets were faster or that the peak intensities were significantly greater at *PSP*, which was a factor of ∼2 closer to the Sun. However, because IS⊙IS/EPI-Hi was turned off for the first several hours of the events, neither the rise nor the peak intensity was observed. As noted in Section 5, the average He intensity at ∼1 MeV nucleon^{-1} was a factor of ∼4 greater at *PSP* than at *ACE* during the period when IS⊙IS/EPI-Hi was making measurements on 2019-110, which might be attributable to a $1/r^2$ dependence of the fluence.

Measurements at *ACE* (Wiedenbeck et al. 2019) indicate the presence of SEP ^{3}He near Earth no more than a few percent of the time in the solar minimum years of 2008-09 and again in 2018-19. However, those observations do not rule out the possibility that the Sun could have been producing ^{3}He-rich SEP events having intensities so low that ^{3}He particles reaching 1 au could not be recognized as belonging to individual SEP events.

We have examined the IS⊙IS/EPI-Hi He isotope data from the first two *PSP* orbits looking for indications of small ^{3}He rate increases that might be due to weak impulsive events. Aside from the 2019-110–111 ^{3}He-rich period discussed in this paper, no other clear indications of ^{3}He increases were found. However, sensitivity of IS⊙IS/EPI-Hi to such increases was limited during these early orbits by the need to identify ^{3}He using pulse height event data, which only represent a sample of the events that are classified on board.

8. Summary and Conclusions

On 2019-110–111, the IS⊙IS energetic particle suite on the *PSP* made its first observations of ^{3}He-rich SEPs. Less than 3 weeks before, *PSP* went through its second perihelion

at a heliocentric radius of 0.17 au. By the time of the ^{3}He-rich SEP observations, the spacecraft had reached 0.46 au. The *PSP* instruments were operating only intermittently at that time because they needed to be turned off while the spacecraft was performing high-speed downlinks of the data that had been collected on its solid-state recorder. During the times when IS☉IS/EPI-Hi was operating, it measured an energetic particle population that was ^{3}He-rich and had the highest intensities of high-energy (>1 MeV nucleon^{-1}) SEP H, He, and heavier ions that had been observed up to that time in the mission. In addition, it made measurements of the only MeV electron events encountered during the first two orbits.

At the time of these observations, *PSP*'s magnetic footpoint at the Sun was close to that of near-Earth spacecraft, including *ACE*. We reported IS☉IS ion and electron measurements, as well as those from the *ACE*/ULEIS and *ACE*/EPAM instruments. ^{3}He/^{4}He ratios measured at both *PSP* and *ACE* were within a factor of ~2 of 0.10, which is $\sim250\times$ the solar wind ratio, but not uncommon in impulsive SEP events. In addition, we presented *SDO*/AIA observations of jets from the active regions associated with the ^{3}He-rich energetic particles and discussed *Wind*/WAVES and *PSP*/FIELDS/RFS observations of type III radio bursts.

There were two active regions, AR 12738 at $\sim$W90 and AR 12739 at $\sim$W70, that could have been magnetically well connected to the two spacecraft. AR 12738 was clearly responsible for the event seen on 2019-110. At the onset time of the 2019-111 event, AR 12738 was behind the west limb; X-rays or other electromagnetic emissions from the low corona were not observable. We showed, however, that this region and other regions with similar Carrington coordinates had been repeated sources of X-ray flares over a period of approximately 7 months, while AR 12739 had been tracked throughout this same time and produced very little X-ray activity until it finally became more active after 2019-130. AR 12739 was visible from *GOES* on 2019-111 but produced no detectable X-ray flares. The only indication that we found that AR 12739 could have been the source of the ^{3}He-rich event on 2019-111 was a jet imaged by *SDO*/AIA (Figure 11, top right panel). We were not able to absolutely exclude AR 12739 as the source, but we regard it as quite unlikely.

The large gaps in the IS☉IS data prevented a detailed comparison of the characteristics of the ^{3}He-rich events detected at *PSP* and at *ACE*, but the incomplete data that are available appear largely consistent. These first IS☉IS observations of ^{3}He-rich SEPs provided a very useful demonstration of some of the suite's capabilities. We also searched the IS☉IS/EPI-Hi data set for small ^{3}He-rich SEP events that were not observable near Earth but might have been detectable closer to the Sun because of the expected strong radial dependence of the intensities of SEP events impulsively released from localized sources. No such population of small events was detected during the first two *PSP* orbits, but the need to use the pulse height event data returned to the ground for identifying ^{3}He limited the sensitivity.

We will be continuing our studies of ^{3}He-rich SEP events and searching for smaller events with the increased sensitivity afforded by onboard He isotope identification as the *PSP* gets progressively closer to the Sun and as Solar Cycle 25 becomes more active. These observations should enable IS☉IS to make significant progress in understanding the acceleration and transport of SEPs close to the Sun.

ORCID iDs

M. E. Wiedenbeck ⓘ https://orcid.org/0000-0002-2825-3128
R. Bučík ⓘ https://orcid.org/0000-0001-7381-6949
G. M. Mason ⓘ https://orcid.org/0000-0003-2169-9618
G. C. Ho ⓘ https://orcid.org/0000-0003-1093-2066
R. A. Leske ⓘ https://orcid.org/0000-0002-0156-2414
C. M. S. Cohen ⓘ https://orcid.org/0000-0002-0978-8127
E. R. Christian ⓘ https://orcid.org/0000-0003-2134-3937
A. C. Cummings ⓘ https://orcid.org/0000-0002-3840-7696
M. I. Desai ⓘ https://orcid.org/0000-0002-7318-6008
D. K. Haggerty ⓘ https://orcid.org/0000-0001-6395-8943
M. E. Hill ⓘ https://orcid.org/0000-0002-5674-4936
C. J. Joyce ⓘ https://orcid.org/0000-0002-3841-5020
A. W. Labrador ⓘ https://orcid.org/0000-0001-9178-5349
O. Malandraki ⓘ https://orcid.org/0000-0002-4751-6835
W. H. Matthaeus ⓘ https://orcid.org/0000-0001-7224-6024
D. J. McComas ⓘ https://orcid.org/0000-0001-6160-1158
R. L. McNutt, Jr. ⓘ https://orcid.org/0000-0002-4722-9166
R. A. Mewaldt ⓘ https://orcid.org/0000-0003-2178-9111
D. G. Mitchell ⓘ https://orcid.org/0000-0003-1960-2119
A. Posner ⓘ https://orcid.org/0000-0003-1572-8734
J. S. Rankin ⓘ https://orcid.org/0000-0002-8111-1444
E. C. Roelof ⓘ https://orcid.org/0000-0002-2270-0652
N. A. Schwadron ⓘ https://orcid.org/0000-0002-3737-9283
E. C. Stone ⓘ https://orcid.org/0000-0002-2010-5462
J. R. Szalay ⓘ https://orcid.org/0000-0003-2685-9801
S. D. Bale ⓘ https://orcid.org/0000-0002-1989-3596
A. W. Case ⓘ https://orcid.org/0000-0002-3520-4041
J. C. Kasper ⓘ https://orcid.org/0000-0002-7077-930X
K. E. Korreck ⓘ https://orcid.org/0000-0001-6095-2490
D. E. Larson ⓘ https://orcid.org/0000-0001-5030-6030
R. J. MacDowall ⓘ https://orcid.org/0000-0003-3112-4201
M. Pulupa ⓘ https://orcid.org/0000-0002-1573-7457
M. L. Stevens ⓘ https://orcid.org/0000-0002-7728-0085

References

Bale, S. D., Goetz, K., Harvey, P. R., et al. 2016, SSRv, 204, 49

Bučík, R., Wiedenbeck, M. E., Mason, G. M., et al. 2018, ApJL, 869, L21

Cliver, E. W. 2009, CEAB, 33, 253

Cohen, C. M. S., Christian, E. R., Cummings, A. C., et al. 2020, ApJS, doi:10.3847/1538-4365/ab4c38

Driesman, A., Hynes, S., & Cancro, G. 2008, SSRv, 136, 17

Fox, N. J., Velli, M. C., Bale, S. D., et al. 2016, SSRv, 204, 7

Geiss, J., & Gloeckler, G. 2003, SSRv, 106, 3

Gold, R. E., Krimigis, S. M., Hawkins, S. E. I., et al. 1998, SSRv, 86, 541

Hill, M. E., Mitchell, D. G., Andrews, G. B., et al. 2017, JGRA, 122, 1513

Joyce, C. J., McComas, D. J., Christian, E. R., et al. 2020, ApJS, doi:10.3847/1538-4365/ab5948

Kallenrode, M. B. 2003, JPhG, 29, 965

Kasper, J. C., Abiad, R., Austin, G., et al. 2016, SSRv, 204, 131

Lemen, J. R., Title, A. M., Akin, D. J., et al. 2012, SoPh, 275, 17

Leske, R. A., Christian, E. R., Cohen, C. M. S., et al. 2020, ApJS, doi:10.3847/1538-4365/ab5712

Malandraki, O. E., & Crosby, N. B. 2018, ASSL, 444, 1

Mason, G. M. 2007, SSRv, 130, 231

Mason, G. M., Gold, R. E., Krimigis, S. M., et al. 1998, SSRv, 86, 409

Mason, G. M., Ng, C. K., Klecker, B., & Green, G. 1989, ApJ, 339, 529

McComas, D. J., Alexander, N., Angold, N., et al. 2016, SSRv, 204, 187

McComas, D. J., Bame, S. J., Barker, P., et al. 1998, SSRv, 86, 563

McComas, D. J., Christian, E. R., Cohen, C. M. S., et al. 2019, Natur, 576, 223

Nitta, N. V., Mason, G. M., Wang, L., Cohen, C. M. S., & Wiedenbeck, M. E. 2015, ApJ, 806, 235

Pesnell, W. D., Thompson, B. J., & Chamberlin, P. C. 2012, SoPh, 275, 3

Pevtsov, A. A. 2016, arXiv:1611.02652

Reames, D. V. 1999, SSRv, 90, 413

Reames, D. V. 2018, SSRv, 214, 61

Ruffolo, D., Khumlumlert, T., & Youngdee, W. 1998, JGR, 103, 20591

Schwadron, N. A., Bale, S., Bonnell, J., et al. 2020, ApJS, doi:10.3847/1538-4365/ab5527

Slocum, P. L., Stone, E. C., Leske, R. A., et al. 2003, ApJ, 594, 592

Stone, E. C., Frandsen, A. M., Mewaldt, R. A., et al. 1998, SSRv, 86, 1

Thompson, W. T. 2006, A&A, 449, 791

Vainio, R., & Afanasiev, A. 2018, ASSL, 444, 45

Wang, L., Krucker, S., Mason, G. M., Lin, R. P., & Li, G. 2016, A&A, 585, A119

Wang, Y. M., Pick, M., & Mason, G. M. 2006, ApJ, 639, 495

Wibberenz, G., & Cane, H. V. 2006, ApJ, 650, 1199

Wiedenbeck, M., Cohen, C., Klassen, A., et al. 2015, Proc. ICRC, 34, 106

Wiedenbeck, M. E., Angold, N. G., Birdwell, B., et al. 2017, Proc. ICRC, 35, 16

Wiedenbeck, M. E., Mason, G. M., McComas, D. J., & Christian, E. R. 2019, Proc. ICRC, 36, 1171